



HAL
open science

Achieving complete reaction while the solid volume increases: A numerical model applied to serpentinitisation

Benjamin Malvoisin, Yury y Podladchikov, Artem V Myasnikov

► To cite this version:

Benjamin Malvoisin, Yury y Podladchikov, Artem V Myasnikov. Achieving complete reaction while the solid volume increases: A numerical model applied to serpentinitisation. *Earth and Planetary Science Letters*, 2021, 563, pp.116859. 10.1016/j.epsl.2021.116859 . hal-03330686

HAL Id: hal-03330686

<https://cnrs.hal.science/hal-03330686>

Submitted on 1 Sep 2021

HAL is a multi-disciplinary open access archive for the deposit and dissemination of scientific research documents, whether they are published or not. The documents may come from teaching and research institutions in France or abroad, or from public or private research centers.

L'archive ouverte pluridisciplinaire **HAL**, est destinée au dépôt et à la diffusion de documents scientifiques de niveau recherche, publiés ou non, émanant des établissements d'enseignement et de recherche français ou étrangers, des laboratoires publics ou privés.

Achieving complete reaction while the solid volume increases: a numerical model applied to serpentinisation

Benjamin Malvoisin^{a,b,*}, Yury Y. Podladchikov^{b,c}, Artem V. Myasnikov^c

^a*Univ. Grenoble Alpes, Univ. Savoie Mont Blanc, CNRS, IRD, IFSTTAR, ISTerre, 38000 Grenoble, France*

^b*ISTE-FGSE, Université de Lausanne, Quartier de la Mouline, Géopolis, CH-1015 Lausanne, Switzerland*

^c*Faculty of Mechanics and Mathematics, Moscow State University, Russian Federation*

Abstract

Solid volume increases during the hydration of mantle rocks. The fluid pathways necessary to feed the reaction front with water can be filled by the low density reaction products. As a result, the reaction front dries out and the reaction stops at low reaction progress. This process of porosity clogging is generally predicted to dominate in reactive transport models, even when processes such as reaction-induced fracturing are considered. These predictions are not consistent with observations at mid-ocean ridges where dense mantle rocks can be completely replaced by low density serpentine minerals. To solve this issue, we develop a numerical model coupling reaction, fluid flow and deformation. High extents of reaction can only be achieved when considering that the increase in solid volume during reaction is accommodated through deformation rather than porosity clogging. The model can generate an overpressure that depends on the extent of reaction and on the boundary conditions. This overpressure induces viscoelastic compaction that limits the extent of the reaction. The serpentinisation rate is therefore controlled by the accommodation of volume change during reaction, and thus by deformation, either induced by the reaction itself or by tectonic processes.

Keywords: serpentinisation, numerical model, reaction rate, tectonic deformation, solid volume increase, fluid pathways, porosity clogging, crystallisation pressure.

1. Introduction

Olivine, the main component of mantle peridotites, hydrates at temperature below ~ 400 °C to form serpentine \pm brucite \pm magnetite \pm hydrogen (Evans, 1977). This so-called reaction of serpentinisation requires fluid transport along
5 pathways often formed by tectonic deformation. In marine geodynamic settings,

*Corresponding author: benjamin.malvoisin@univ-grenoble-alpes.fr

the fluid pathways include detachment faults at slow-spreading mid-ocean ridges (Cannat, 1993; Escartín et al., 2008; Rüpke and Hasenclever, 2017), bend-faults at ocean trenches (Ranero et al., 2003; Van Avendonk et al., 2011), and extensional faults at passive margins (Bayrakci et al., 2016). Here we focus on
10 serpentinisation during mantle rock exhumation in the footwall of detachment faults at slow spreading mid-ocean ridges.

Serpentinisation induces changes in the behaviour of the oceanic lithosphere due to strong differences in the physico-chemical properties of the reactants and the products. Serpentine content above $\sim 10\%$ reduces the rock strength by
15 decreasing the friction coefficient from 0.6 to ~ 0.4 (Escartín et al., 1997) with consequences on the rheology of the detachment faults active at mid-ocean ridges (Bickert et al., 2020). Magnetite is a ferrimagnetic mineral with a magnetisation four orders of magnitudes higher than olivine (Malvoisin et al., 2012b). Its precipitation during serpentinisation can generate magnetic anomalies on the
20 seafloor (Szitkar et al., 2014). Hydrogen is an energy source for chemosynthetic organisms and participates in the abiotic synthesis of organic compounds possibly involved in the origin of life (Russell et al., 2010; McCollom and Seewald, 2013). Serpentinisation is also an exothermic reaction possibly modifying the heat budget at mid-ocean ridges (Macdonald and Fyfe, 1985). Predicting the
25 evolution of the oceanic lithosphere thus requires to model the rate and the extent of serpentinisation at mid-ocean ridges.

Serpentinisation is already modelled at the kilometre scale to investigate its influence on hydrothermal circulation, heat budget and geodynamics (Emmanuel and Berkowitz, 2006; Delescluse and Chamot-Rooke, 2008; Iyer et al.,
30 2010; Bickert et al., 2020). Reaction rate is assumed to be controlled by a single process in these models. Emmanuel and Berkowitz (2006) and Iyer et al. (2010) used a law derived from experiments of olivine powder hydration (Martin and Fyfe, 1970) whereas Bickert et al. (2020) relate serpentinisation rate to the shear deformation. It remains unclear which assumption should be preferred to model serpentinisation at large scale. Moreover, the used models are
35 either incompressible, considering a constant porosity or using a parametrized law for the evolution of porosity. Such approaches are justified by the need to use simplifying assumptions when modelling processes at different time and space scales. However, they cannot take into account the impact of hydration
40 on density and porosity whereas these parameters strongly modify deformation and fluid flow.

Volume change during reaction is the key parameter for modelling the couplings between reaction, deformation and fluid flow. Serpentinisation induces a change in solid volume ($\Delta V/V$) of $\sim 50\%$ in a closed system (Macdonald and Fyfe, 1985; O’Hanley, 1992). Mass transfer through aqueous species transport can reduce the increase in solid volume (Thayer, 1966; Carmichael, 1987; Fletcher and Merino, 2001). However, Malvoisin et al. (2020b) and Klein and Le Roux (2020) measure $\Delta V/V$ in natural samples and in experiments close to the
45 theoretical value for reaction in a closed system, suggesting that mass transfer is limited, at least during the incipient stage of the reaction. The serpentinisation
50 rate directly depends on the evolution of the fluid pathways during reaction.

They initially form by thermal cracking (Demartin et al., 2004; Boudier et al., 2010) or tectonic deformation (Rouméjon et al., 2015), and then evolve during reaction as a consequence of $\Delta V/V$. The precipitation of reaction products in
55 the pores reduces the permeability by several orders of magnitude (Godard et al., 2013; Farough et al., 2015). However, a porosity is observed at the nanoscale in serpentinized peridotites (Tutolo et al., 2016). Fluid pathways could thus be preserved during reaction, even though this should be confirmed with the acquisition of data on pore connectivity at the nanoscale. The positive change
60 in volume during reaction also generates stresses (i.e. crystallisation pressure) sufficient to fracture the rock (Jamtveit et al., 2009; Kelemen and Hirth, 2012; Plümper et al., 2012; Malvoisin et al., 2017).

The positive $\Delta V/V$ is considered in some models of serpentinisation. It induces stress build-up and crack generation in the models of reaction-induced
65 fracturing (Rudge et al., 2010; Ulven et al., 2014; Shimizu and Okamoto, 2016; Malvoisin et al., 2017; Zhang et al., 2019). These models predict an increase in reactive surface area during reaction and reproduce the mesh microtexture observed in natural samples. However, they either do not take into account Darcian flow, or they do not conserve fluid mass, and are consequently not able
70 to quantitatively model porosity evolution during reaction (Evans et al., 2020). Reactive transport models such as TOUGHREACT (Xu et al., 2011) incorporate the volumetric effect of reaction on transport properties. They predict a strong reduction in porosity during reaction inducing a positive $\Delta V/V$, preventing the achievement of the high extents of reaction measured in natural samples
75 (Liu et al., 2019; Marini, 2007). This limitation probably arises from the omission in these models of mechanisms responsible for fluid pathways generation or preservation. Evans et al. (2020) consider reaction-induced fracturing in a model combining reaction and fluid flow. They were able to model the effect on fluid pathway evolution of the competition between cracking and porosity
80 clogging. However, high extents of reaction ($> 60\%$) are only achieved in the cracks with limited hydration in the rock groundmass. The main issue regarding serpentinisation modelling thus consists in being able to predict the high extents of reaction observed in the natural samples.

The present contribution aims at proposing a new model of serpentinisation
85 addressing this issue. We derive a new set of equations to model the couplings between reaction, deformation and fluid flow. Based on observations in natural samples, we consider that the solid volume increase is accommodated through deformation rather than porosity clogging. The new model is applied to serpentinisation at mid-ocean ridges in the footwall of a detachment fault. We model
90 fluid-rock interaction during hydrothermal circulation with a one-dimensional numerical model. The impact of the parameter values on the model predictions is explored. On the contrary to previous modelling attempts, the new approach allows high extents of reaction to be reached and reaction-induced pressure increase to be predicted. The model is finally used to discuss the processes
95 controlling the serpentinisation rate.

2. Modelling the couplings between reaction, deformation and fluid flow

The model considers a porous matrix of dunite reacting with water in the stability field of serpentine + brucite. Serpentinisation is assumed to be iso-chemical except for the addition of water based on the study of Malvoisin et al. (2020b). Si, Mg and Fe are thus not transported as aqueous species between the model grid points. We use here a two-phase continuum medium approach by defining macroscopic properties such as porosity and extent of reaction for a mineralogical assemblage potentially composed at each grid point of both olivine and its reaction products. This approach is valid at a scale larger than the olivine grain size so that the rock properties can be averaged over a significant number of grains. Olivine grains reacting during serpentinisation have a typical size of 100 μm (Malvoisin et al., 2017). The model can thus be used from a scale of ~ 1 mm. The model parameters and their values are given in Table 1. The model is based on the model developed in Malvoisin et al. (2015) and in Omlin et al. (2017). The thermodynamic admissibility of the systems of equations derived below is also verified following the procedure described in Yarushina and Podladchikov (2015) (see supplementary materials for details).

The mass conservation equations can be written for the total system as:

$$\frac{\partial (\rho_w \phi + \rho_s (1 - \phi))}{\partial t} + \nabla_j (\rho_w \phi v_w^j + \rho_s (1 - \phi) v_s^j) = 0 \quad (1)$$

and for the dry solid as:

$$\frac{\partial (\rho_s (1 - X_s) (1 - \phi))}{\partial t} + \nabla_j (\rho_s (1 - X_s) (1 - \phi) v_s^j) = 0 \quad (2)$$

where X_s , ϕ , ρ , v^j and ∇_j are the mass fraction of water bound to the solid, the porosity, the density, the j components of the velocity vector and the j components of the del operator, respectively. The solid properties are denoted with a subscript s , and the water properties are denoted with a subscript w . This particular choice of two independent mass conservation equations is motivated by their independence on (de)hydration reactions and the absence of reaction-related source terms.

The conservation of fluid momentum is modelled with the Darcy's law:

$$\phi (v_w^j - v_s^j) = -\frac{k_\phi}{\eta_w} (\nabla_j P_w + \rho_w g e_z^j) \quad (3)$$

where k_ϕ is the permeability, η_w is the fluid viscosity, P_w is the fluid pressure and e_z^j are the components of an upward directed unit vector. Combining equation 3 with equations 1 and 2 allows water velocity to be eliminated.

The changes in density are modelled by introducing compressibilities. The solid compressibility and the density change during reaction contribute to the

Symbol	Definition	Unit	Value
L	Length of the numerical model	m	$10^{-1} - 10^2$
ρ_w	Water density	$kg.m^{-3}$	1000 (at 200°C and 50 MPa)
ρ_s	Solid density	$kg.m^{-3}$	3300 (initial value)
v_w^j	Velocity of water	$m.s^{-1}$	
v_s^j	Velocity of the solid	$m.s^{-1}$	
X_s	Mass fraction of water bound in the solid	None	0 (initial value)
X_{seq}	Mass fraction of water bound in the solid at the equilibrium	None	0.126*
ϕ	Porosity	None	
ϕ_0	Initial porosity	None	0.01
ϕ_p	Porosity above which a porous rock has the same reactive surface area as a powder	None	0.38
k_ϕ	Permeability	m^2	$10^{-20} - 10^{-16}$
η_w	Water viscosity	$Pa.s$	10^{-4}
g	Gravity acceleration	$m^2.s^{-1}$	9.81
e_z^j	Unit vector along upward directed z-axis	None	
η_ϕ	Pore viscosity	$Pa.s$	$10^{17} - 10^{20}$
τ	Characteristic time for reaction	s	$10^7 - 10^9$
P_w	Fluid pressure	Pa	50.10^6 (initial value)
P_s	Solid pressure	Pa	50.10^6 (initial value)
\bar{P}	Total pressure (fluid + solid)	Pa	50.10^6 (initial value)
β_d	Drained compressibility	Pa^{-1}	7.10^{-10}
β'_s	Solid compressibility measured in an unjacketed test	Pa^{-1}	$1.5.10^{-11}$
β_w	Fluid compressibility defined in equation 6	Pa^{-1}	10^{-9} *
β_{ef}	Effective compressibility in front of P_w	Pa^{-1}	
β_{et}	Effective compressibility in front of \bar{P}	Pa^{-1}	
β_{sr}	Change in solid density due to reaction (defined in equation 4)	None	1.7*
ϵ_V	Dilatational strain rate	s^{-1}	$10^{-14} - 10^{-9}$
ξ	Extent of reaction ($\xi = \frac{X_s}{X_{seq}}$)	None	0 - 1
$\dot{\xi}$	Serpentinisation rate	s^{-1}	
t_{80}	Time to reach 80 % of extent of reaction	s	

Table 1: Symbols used in the mathematical model. *: parameter value calculated with Perple-X (Connolly, 2005)

130 solid density evolution:

$$\frac{1}{\rho_s} \frac{d\rho_s}{dt} = \beta'_s \left(\frac{dP_s}{dt} - \frac{\bar{P} - P_w}{(1 - \phi)^2} \frac{d\phi}{dt} \right) - \beta_{sr} \frac{1}{1 - X_s} \frac{dX_s}{dt} \quad (4)$$

where β'_s is the solid compressibility measured in an unjacketed test, β_{sr} is the density change associated with hydration (X_s modification), and P_s is the solid pressure. $\frac{d}{dt}$ is the material derivative of the solid phase defined as $\frac{d}{dt} = \frac{\partial}{\partial t} + v_s^j \nabla_j$. P_s is combined with P_w to calculate the total pressure (\bar{P}) as:

$$\bar{P} = \phi P_w + (1 - \phi) P_s \quad (5)$$

135 The change in fluid density is calculated by introducing the fluid compressibility (β_w):

$$\frac{1}{\rho_w} \frac{d_w \rho_w}{dt} = \beta_w \frac{d_w P_w}{dt} \quad (6)$$

where $\frac{d_w}{dt}$ is the material derivative of the water defined as $\frac{d_w}{dt} = \frac{\partial}{\partial t} + v_w^j \nabla_j$

Finally, the change in composition (X_s) is modelled with a first-order kinetic law:

$$\frac{dX_s}{dt} = \left(\frac{\phi}{\phi_p} \right)^{2/3} \frac{X_{seq} - X_s}{\tau} \quad (7)$$

140 where τ is the characteristic time for reaction and X_{seq} is the water mass fraction bound to the solid at the equilibrium, that is in the serpentine + brucite assemblage. The evolution of reactive surface area during reaction is modelled as a function of porosity with the geometrical relationship proposed by Lichtner (1988) and Kieffer et al. (1999). ϕ_p is the minimum porosity for which a porous
145 rock has the same reactive surface area than a powder. We use a value of 0.38 in the following based on the experimental results of Llana-Fúnez et al. (2007).

Equations 1, 2, 3, 4, 6, 5 and 7 form a system of nine equations in thirteen unknowns, 7 scalars (ρ_w , ρ_s , ϕ , X_s , P_w , P_s and \bar{P}) and 6 vector components (v_w^j and v_s^j). Solving this system of equations thus requires four additional
150 equations.

The conservation of total momentum could first be used (Malvoisin et al., 2015) but this would require to solve for shear stress evolution which is beyond the scope of this study. We thus explore the behaviour of the system of equations for two cases: (i) a constant solid volume ($\nabla_j v_s^j = 0$); (ii) a constant total
155 pressure ($\bar{P} = constant$). These approximations correspond to idealized systems in which reaction-induced change in volume is either not accommodated (i) or fully accommodated (ii) by deformation. The behaviour of a real system is expected to be intermediate between these two extreme cases. Nevertheless, these approximations provide maximum estimates for total pressure variation
160 during reaction (i) and reaction-induced deformation (ii).

The last equation necessary to close the system of equations is the equation for solid deformation. We show below why this equation plays a key role for

modelling solid volume change during reaction. We first present the classical form of this equation usually used in reactive transport models. We then show
165 how it should be modified to take into account observations at the nanoscale of limited mass transfer during serpentinitisation.

2.1. Classical approach

The classical approach refers here to models in which reaction-induced deformation is not considered in the equations for solid deformation. This approach
170 is used in most of the models considering the couplings between reaction and deformation (Balashov and Yardley, 1998; Xu et al., 2011; Tian and Ague, 2014; Malvoisin et al., 2015; Tian et al., 2018; Malvoisin et al., 2020a; Evans et al., 2020; Schmalholz et al., 2020). With the classical approach, solid deformation is modelled independently from reaction for example with a visco-elastic rheology
175 (Yarushina and Podladchikov, 2015):

$$\nabla_j v_s^j = -\beta_d \frac{d\bar{P}}{dt} + (\beta_d - \beta'_s) \frac{dP_w}{dt} - \frac{\bar{P} - P_w}{(1 - \phi) \eta_\phi} \quad (8)$$

where β_d and η_ϕ are respectively, the drained compressibility and the pore viscosity.

Re-arranging equations 1, 2, 3, 4, 5, 6 and 7 with additional equation 8 provides a closed system of three equations describing the system evolution
180 with three unknown scalar functions, porosity (ϕ), fluid pressure (P_w) and mass fraction of water in the solid (X_s):

$$\left\{ \begin{array}{l} \frac{dX_s}{dt} = \left(\frac{\phi}{\phi_p} \right)^{2/3} \frac{X_{seq} - X_s}{\tau} \\ \nabla_j \frac{k_\phi}{\eta_w} (\nabla_j P_w + \rho_w g e_z^j) = -\beta_{e_t} \frac{d\bar{P}}{dt} + \beta_{e_w} \frac{dP_w}{dt} - \frac{\bar{P} - P_w}{(1 - \phi) \eta_\phi} + \left(\frac{\rho_s}{\rho_w} - (1 + \beta_{sr}) \right) \frac{1 - \phi}{1 - X_s} \frac{dX_s}{dt} \\ \frac{1}{(1 - \phi)} \frac{d\phi}{dt} = \left(\beta_{e_t} - \frac{\beta'_s \phi}{1 - \phi} \right) \left(-\frac{d\bar{P}}{dt} + \frac{dP_w}{dt} \right) - \frac{\bar{P} - P_w}{(1 - \phi) \eta_\phi} - \frac{1 + \beta_{sr}}{1 - X_s} \frac{dX_s}{dt} \end{array} \right. \quad (9)$$

where β_{e_t} and β_{e_w} are the total and fluid effective compressibilities, respectively, defined as

$$\beta_{e_t} = \beta_d - \beta'_s, \quad (10)$$

and

$$\beta_{e_w} = \beta_{e_t} + \phi (\beta_w - \beta'_s). \quad (11)$$

Reactive terms appear in the fluid pressure and the porosity evolution equations in 9. This implies that volume change during reaction is accommodated
185 through precipitation in the pores and fluid pressure variation. Mineralogical reactions in the presence of fluid proceed through four steps: the transport of fluid up to the primary minerals, the dissolution of the primary minerals, the transport of aqueous species and the precipitation of the secondary minerals

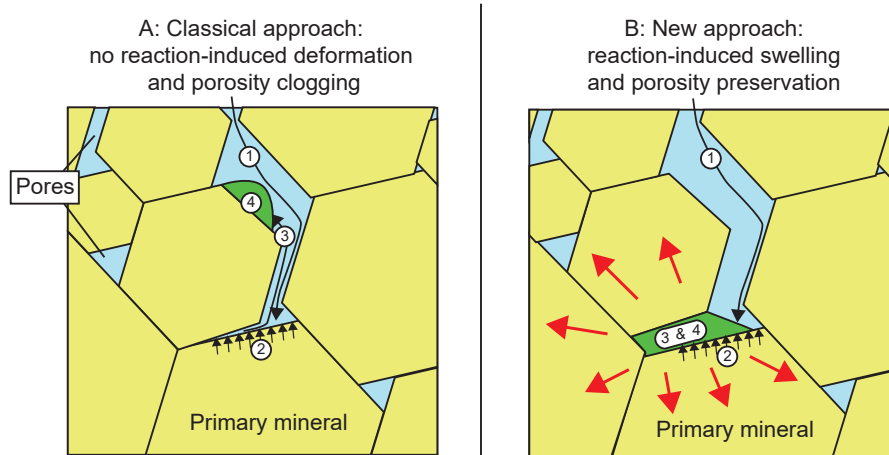


Figure 1: The two types of models to link reaction, porosity evolution and solid deformation. Mineralogical reactions in the presence of fluid can be decomposed in four steps: fluid transport in the pore network (1); primary mineral (in yellow) dissolution (2); aqueous species transport (3); and secondary phase (in green) precipitation (4). A: the classical approach consists in considering that aqueous species are transported up to the pores where precipitation occurs. This process does not generate deformation directly. B: the new approach proposed here is based on observations at the nanoscale showing that aqueous species transport can be limited to a scale of less than 100 nm. As a result, the reaction products do not precipitate in the pores but at the surface of the primary mineral. This implies that reaction induces rock deformation (i.e. swelling; red arrows).

190 (Figure 1). Modelling fluid-mediated reactions thus requires to assume that
 aqueous species transport occurs. We do not consider this process in our equa-
 tions, implying that the occurrence of aqueous species transport is restricted to
 a scale below the spacing of the grid points in our model (< 1 mm). However, we
 directly relate here porosity evolution to reaction. This implicitly requires that
 195 mass transfer efficiently occurs at least at the micrometer scale from the olivine
 surface up to the pores (Figure 1A). This latter assumption may not be veri-
 fied during hydration reactions as suggested by observations in natural samples
 (Beard et al., 2009; Boudier et al., 2010; Malvoisin et al., 2020b). We propose
 in the following a way to take into account these observations by modifying
 200 equation 8.

2.2. A new approach: reaction-induced swelling

At the submicrometre scale, Beard et al. (2009) and Malvoisin et al. (2020b)
 report reaction products dominated by a serpentine + brucite mixture with a
 composition similar to olivine except for the addition of water. Boudier et al.
 205 (2010) show the presence of a ~ 100 nm thick zone coating the olivine surface,
 and composed of pre-hydrated olivine. Serpentinisation is thus isochemical at
 least at the hundred of nanometre scale with limited aqueous species transport,
 probably by diffusion at grain boundaries (Tutolo et al., 2016) (Figure 1B). Such

210 a replacement process with limited transport is not expected to significantly modify the existing pores. This implies that the positive change in solid volume occurring during reaction is not accommodated by mass transfer up to the pores but rather by deformation (Figure 1B). All these observations can be taken into account by modifying equation 8 such that porosity evolution does not depend on volume change during reaction:

$$\nabla_j v_s^j = -\beta_d \frac{d\bar{P}}{dt} + (\beta_d - \beta'_s) \frac{dP_w}{dt} - \frac{\bar{P} - P_w}{(1 - \phi) \eta_\phi} + \frac{1 + \beta_{sr}}{1 - X_s} \frac{dX_s}{dt} \quad (12)$$

215 The last term in equation 12 is the deformation induced by solid volume change. With this new equation for solid momentum conservation, a new closed system of three equations for three unknown functions, ϕ , P_w and X_s is obtained by also using equations 1, 2, 3, 4, 5, 6 and 7:

$$\left\{ \begin{array}{l} \frac{dX_s}{dt} = \left(\frac{\phi}{\phi_p} \right)^{2/3} \frac{X_{seq} - X_s}{\tau} \\ \nabla_j \frac{k_\phi}{\eta_w} (\nabla_j P_w + \rho_w g e_z^j) = -\beta_{e_t} \frac{d\bar{P}}{dt} + \beta_{e_w} \frac{dP_w}{dt} - \frac{\bar{P} - P_w}{(1 - \phi) \eta_\phi} \\ \quad + \left(\frac{\rho_s (1 - \phi)}{\rho_w} + \phi (1 + \beta_{sr}) \right) \frac{1}{1 - X_s} \frac{dX_s}{dt} \\ \frac{1}{(1 - \phi)} \frac{d\phi}{dt} = \left(\beta_{e_t} - \frac{\beta'_s \phi}{1 - \phi} \right) \left(-\frac{d\bar{P}}{dt} + \frac{dP_w}{dt} \right) - \frac{\bar{P} - P_w}{(1 - \phi) \eta_\phi} \end{array} \right. \quad (13)$$

2.3. Numerical methods, initial set-up and parameters

220 The numerical model aims at determining the conditions necessary to reach high reaction progress during serpentinisation at mid-ocean ridges. We build a simple idealized model for fluid-rock interaction during hydrothermal circulation in exhumed mantle rocks. We do not consider shear deformation and the strong changes in rock composition occurring during extensive alteration. The model
225 thus rather applies to a region located outside the shear zones involved in exhumation in the footwall of a detachment fault. We consider a one-dimensional domain of length L undergoing serpentinisation at $200^\circ C$ and 50 MPa (initial fluid and total pressures). We impose a constant fluid pressure of 50 MPa at the model boundaries during simulation. The domain is assumed horizontal so that
230 gravity terms can be neglected. It is initially exclusively composed of olivine (dunite; $X_s = 0$). The initial porosity is of $\phi_0 = 0.01$ to allow for fluid transport and reaction initiation. We predict the evolution of porosity, pressures and rock hydration degree with the systems of equations 9 and 13 for a wide range of model parameter values.

235 The numerical scheme consists in solving nondimensional versions of equations 9 and 13 with an explicit algorithm using pseudotransient iterations Kelley and Keyes (1998). This algorithm is validated for the system of equations 9 by

reproducing an analytical solution in Omlin et al. (2017). We also produce an analytical benchmark for the system of equations 13. The algorithm is validated
 240 for this system of equations by reproducing an analytical prediction (see the derived analytical solution in the supplementary materials). The non-dimensional equations are obtained by choosing the model scale as the length scale ($\delta = L$), the inverse of the compressibility as the pressure scale ($p^* = \frac{1}{\beta_{ef0}}$) and the characteristic time for viscous compaction as the time scale ($t^* = \frac{\eta_\phi}{p^*}$). This
 245 leads to the introduction of two nondimensional numbers describing the system behaviour : the Dahmköhler number comparing the characteristic times for viscoelastic relaxation and for reaction ($Da = \frac{\beta_{ef0}\eta_\phi}{\tau}$); the Deborah number comparing the characteristic times for viscoelastic relaxation and for viscous compaction ($De = \sqrt{\frac{k_\phi\eta_\phi}{\eta_w L^2}}$). The non-dimensional systems of equations solved
 250 in the numerical models can be found in the supplementary materials. For clarity, we present the following results with dimensional quantities.

The values of the parameters used in the model are given in Table 1. Some parameters such as compressibility are well-constrained. β_w is calculated with Perple_X (Connolly, 2005) by computing the derivative of ρ_w with pressure at
 255 $200^\circ C$ and 50 MPa. We also use Perple_X to compute the change in solid density as a function of X_s that is used to calculate β_{sr} . For the other less constrained parameters, we provide in the following ranges of possible values which are used to compute the Da and De values to be used in the simulations.

Observations in natural samples reveal that preferred fluid pathways separate 10 cm- to 100 m-wide domains undergoing serpentinisation (Rouméjon
 260 et al., 2015). We use this size range as the length of the model (L). Permeability measured during fluid flow experiments on peridotite takes values comprised between 10^{-20} and $10^{-16} m^2$ (Godard et al., 2013; Farough et al., 2015). Pore viscosity spans over four orders of magnitude (10^{17} to $10^{20} Pa.s$; (Hilairret et al.,
 265 2007)). The characteristic time for dunite serpentinisation are calculated for an initial olivine grain size of $100 \mu m$ based on kinetic laws determined with experiments on powders. The main parameter controlling reaction rate is the fluid composition. The slower rates are measured in experiments using pure water ($\tau = 2.10^8 s$) (Malvoisin et al., 2012a) whereas the faster rates are measured with
 270 alkaline fluids ($\tau = 10^7 s$) (Lafay et al., 2012). We use in the following τ values comprised between $10^7 s$ and $10^9 s$. These estimates of parameters are used to determine Da and De values ranging from $10^{-1.15}$ to $10^{3.8}$ and $10^{-1.5}$ to 10^5 , respectively. For each system of equations, we perform simulations with the two assumptions of constant solid volume (i) and constant total pressure (ii). We
 275 run 930 simulations at various De and Da values for each pair of solved equations/assumption (4 x 930 simulations in total). The simulations are stopped when the minimum porosity is below 10^{-15} or when the maximum extent of reaction is above 99 %.

2.4. Porosity clogging with the classical approach

280 We first use the system of equations 9 to model serpentinisation. Reaction leads to fluid pressure decrease due to water consumption by reaction. This

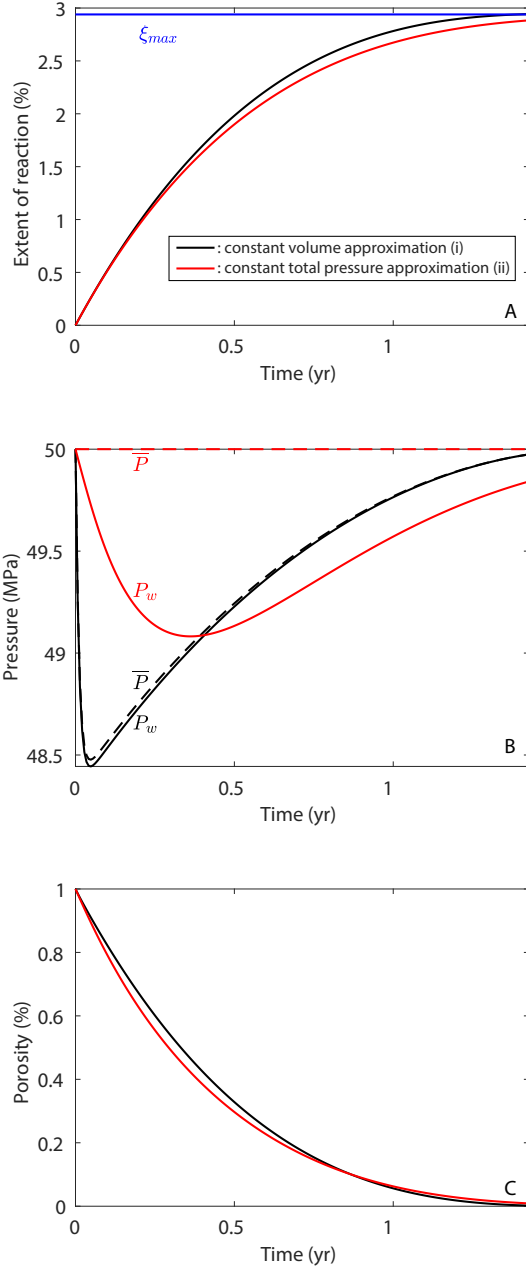


Figure 2: Results of simulations using the classical approach (equations 7 and 9). The evolutions with time of extent of reaction (A), fluid pressure (plain line) and total pressure (dashed line) (B), and porosity (C) are displayed. The models displayed with black and red lines consider a constant volume (i) or a constant total pressure (ii) for closing the system of equations, respectively. The blue line in subpanel A corresponds to the maximum extent of reaction predicted for a non-deforming solid matrix (ξ_{max} ; see text for details). The models are run with $k_\phi = 10^{-19} m^2$, $L = 10m$, $\tau = 5.10^7 s$ and $\eta_\phi = 10^{18} Pa.s$ ($De = 3$; $Da = 14$)

decrease highly depends on the De and Da numbers used in the simulations when a constant solid volume (i) is assumed (Figure S2B). At high De and low Da , P_w variations are limited to several megapascals (Figure 2) whereas, at low De and high Da , it can reach several tens of megapascals (Figure S2). The water vapor pressure at 200 °C (1.6 MPa) can even be achieved. The model does not take into account the effect of vaporisation on density evolution and is thus not relevant for fluid pressures below the water vapor pressure. The fluid pressure decrease is limited to less than 3 MPa when a constant total pressure (ii) is used (Figures 2 B and S3 B). The difference between fluid and total pressure indeed drives viscoelastic compaction, limiting fluid pressure variations relative to total pressure. For all the parameter values investigated here, the model predicts a similar decrease of the reaction rate due to porosity clogging by reaction products (Figures 2 A, S2 A and S3 A). The reaction ultimately stops when the porosity and the reactive surface area are zero. The maximum extent of reaction reached in the simulations is $\xi_{max} = 3\%$. The maximum reaction extent can be predicted by integrating the porosity evolution equation in the system of equation 9 when assuming no deformation and reaction thus limited by the free space initially available (ϕ_0). The obtained expression is $\xi_{max} = \frac{\phi_0}{X_{seq}(1+\beta_{sr})}$ giving a value of 2.94% for $\phi_0 = 0.01$, consistent with the model predictions. This expression of ξ_{max} also provides the minimum initial porosity required to completely serpentinise a rock with the model based on equations 9. We calculate here a minimum initial porosity of 34 %.

2.5. Complete serpentinisation with reaction-induced deformation

The results of numerical modelling with equations 13 significantly depend on the assumption used for closing the system of equations. When assuming a constant solid volume (i), the evolutions of extent of reaction and porosity are similar to the classical approach. The extent of reaction reaches a maximum close to ξ_{max} (Figures 3 A and S4 A) as the porosity decreases to become zero (Figures 3 C). The mechanism of porosity decrease is however different since it is due to mechanical closure here whereas it is due to the precipitation of reaction products in the simulations performed with the classical approach. The driving force for viscoelastic compaction is the total pressure increase as a result of solid volume increase during reaction (Figure 3 C). We calculate a maximum total pressure increase of 14 MPa along a segment spanning from $Da = 10$ and $De = 10^{1.5}$ to $Da = 10^4$ and $De = 10^3$ in Figure S4 B. This indicates that reaction-induced pressure increase is favored by a high reaction rate, a high viscosity and/or a low effective compressibility.

We observe two types of behaviour when assuming a constant total pressure (ii). At high Da and low De , porosity clogging occurs as a result of mechanical compaction as observed with assumption (i) (Figure S5). The final extent of reaction is close to ξ_{max} . At low Da and high De , the porosity and the fluid pressure only change during simulation by less than 0.5 % and several megapascals, respectively (Figure 3 E and F). Fluid pathways are thus preserved, and the extent of reaction reaches 100 % (Figures 3 D and S5 A). The solid volume

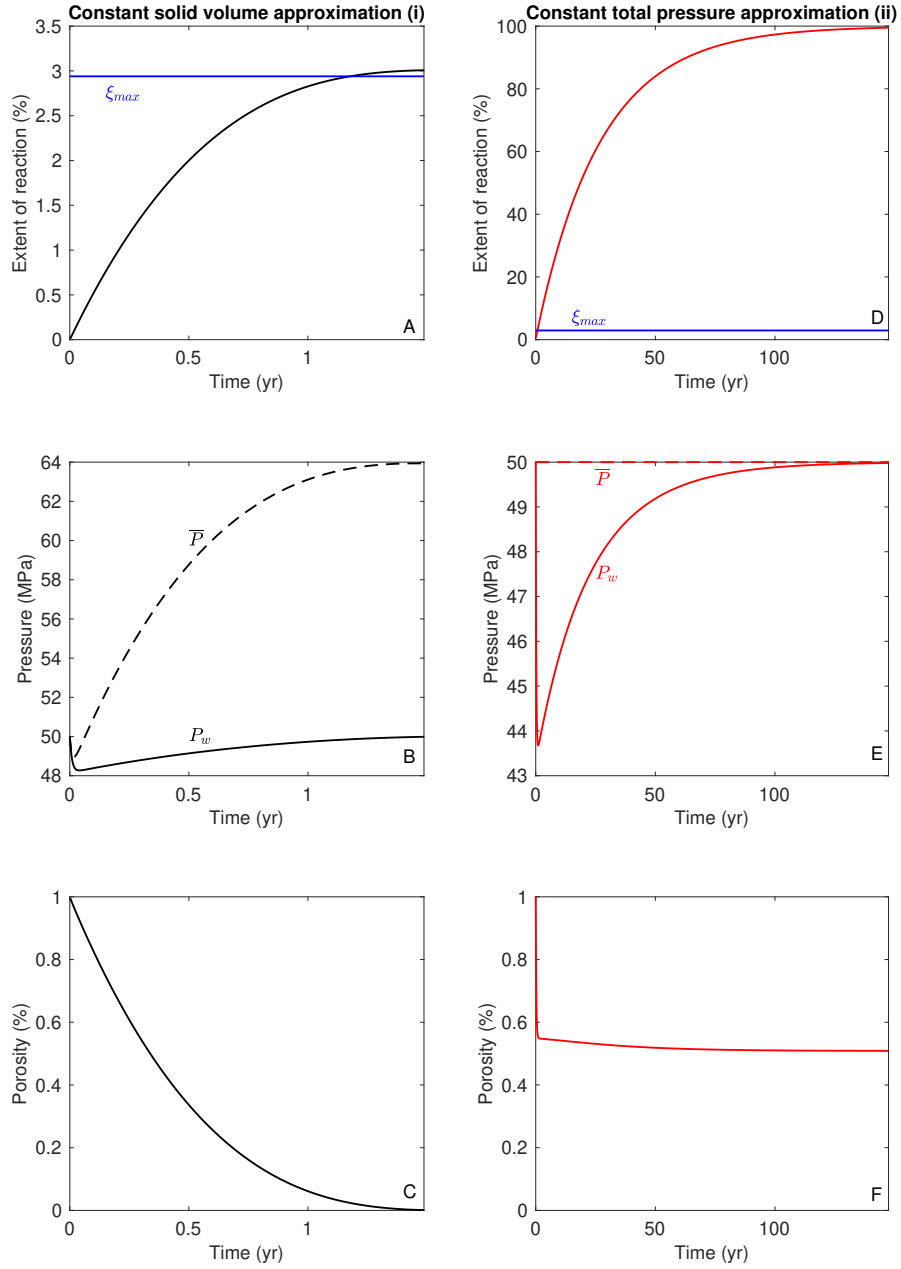


Figure 3: Results of the reaction-induced deformation numerical model (equations 7 and 13) when assuming a constant solid volume (A, B and C) or a constant total pressure (D, E and F). The evolutions with time of extent of reaction (A and D), fluid pressure (plain line) and total pressure (dashed line) (B and E), and porosity (C and F) are displayed. The blue line in subpanels A and D corresponds to the maximum extent of reaction predicted for a non-deforming solid matrix (ξ_{max} ; see text for details). The model is run with $k_\phi = 10^{-19} m^2$, $L = 10m$, $\tau = 5.10^7 s$ and $\eta_\phi = 10^{18} Pa.s$

increase is accommodated by the expansion of the rock matrix. As porosity is rather constant during reaction, the duration of the reaction only depends on τ and ϕ_0 according to equation 7. The simulation displayed in Figure 3 reaches for example completion after approximately 150 yr.

330 3. Discussion and conclusion

Several numerical approaches have been used to model serpentinitisation. Most of them investigate the influence of positive volume increase during reaction on fluid pathways formation (Rudge et al., 2010; Ulven et al., 2014; Malvoisin et al., 2017; Zhang et al., 2019). Nevertheless, the most complete
335 models coupling reaction, stress variation, fluid flow and permeability do not produce complete serpentinitisation in the entire rock (Evans et al., 2020). Reactive transport models such as TOUGHREACT (Xu et al., 2011) also fail to reach high extents of reaction while the solid volume increases during reaction (Paukert, 2014). All these models are based on the same principle as the clas-
340 sical approach detailed here in section 2.1 with a decoupling of reaction and deformation. Positive volume increase can only be accommodated by precipitation in the pores. Mass transfer is assumed to occur at least between the surface of the reacting primary minerals and the pores. The fluid pathways are rapidly clogged, leading to the stop of the reaction if the initial porosity is below $\sim 30\%$
345 (Figure 2). The consumption of fluid by the reaction leads to a decrease in fluid pressure which can reach several tens of megapascals (Figure 2). Evans et al. (2020) predict a similar behaviour but they consider an additional mechanical feedback between fluid pressure variation and tensile failure. This latter coupling allows porosity to be generated in the fractures as fluid pressure decreases
350 whereas the model proposed here only allows viscoelastic compaction to occur. However, the generated porosity is not sufficient to reach high extents of reaction outside the cracks (Evans et al., 2020). These model predictions are not consistent with the observations in natural samples in which extents of reaction above 60 % are commonly measured (Oufi, 2002).

355 The observations of Beard et al. (2009), Boudier et al. (2010) and Malvoisin et al. (2020b) indicate that reaction proceeds locally with mass transfer limited to the submicrometric scale. Positive volume change is thus not accommodated by precipitation, probably due to a slow transport of the aqueous species. The only other way to account for positive volume change in a closed system is to
360 introduce solid volume change in the equation for solid deformation (equation 12). Deriving the change in porosity with this latter equation (last equation in 13) provides an equation without reactive terms, that is without porosity clogging. The modification of equation 12 thus allows for accommodating positive change in solid volume through reaction-induced deformation rather than
365 precipitation in the pores. We solve the system of equations by considering two extreme cases, either no solid volume change (e.g. volume-controlled) or constant total pressure (e.g. stress-controlled).

Reaction is controlled by deformation in our model. If the rock can freely deform by assuming negligible shear stresses (i.e. stress-controlled simulations

370 (ii), a maximum serpentinisation rate ($\dot{\xi}_{max}$) is estimated since shear deformation can only delay the volumetric expansion. $\dot{\xi}_{max}$ depends only on τ and is thus controlled by dissolution and precipitation occurring at the olivine surface (Figures 3 and S5). Complete reaction is achieved in less than 1000 yr, in agreement with previous estimates based on experimental data and reaction-induced
 375 fracturing modelling (Malvoisin et al., 2017). The rock expands by approximately 50 % with consequences for surface uplift and large scale deformation at mid-ocean ridges and in subduction zones (Germanovich et al., 2012).

If deformation is not allowed (i.e. volume-controlled simulations (i)), the serpentinisation rate is zero and the reaction does not reach completion (Figures 3 and S4). We refine the estimation of the minimum reaction rate ($\dot{\xi}_{min}$)
 380 in the following by considering volumetric expansion associated with tectonic deformation which is the main process of deformation at mid-ocean ridges (Cannat, 1993). Tectonic deformation is partitioned between dilatational and shear strains. Microstructural observations indicate that strain in detachment faults
 385 is accommodated by crystal-plastic flow and diffusive mass transfer in multiple shear zones (Schroeder and John, 2004; Boschi et al., 2006). Reaction-softening associated with talc formation promotes shear strain localisation, suggesting that shear deformation accommodates a significant proportion of the deformation. However, this proportion is difficult to quantify since most numerical models of mantle rock exhumation at mid-ocean ridges are incompressible (Behn and
 390 Ito, 2008; Bickert et al., 2020). The model developed here is one-dimensional and does not allow for shear deformation to be modelled. Moreover, volume increase during reaction can only be accommodated by expansion. As a result, we only consider dilatational strain in the following by introducing a constant
 395 rate of expansion in the model ($\nabla_j v_s^j = \epsilon_V^j$ with ϵ_V^j a constant dilatational strain rate imposed by tectonics). Our model is thus not able to probe all the complex interactions between tectonic deformation and serpentinisation at mid-ocean ridges. However, it allows determining the conditions for which tectonic expansion is slower than volume increase induced by dissolution/precipitation
 400 (tectonic-controlled versus dissolution/precipitation-controlled rate).

Simulations performed with several imposed dilatational strain rates indicate that the serpentinisation rate is first equal to a high rate controlled by dissolution and precipitation and rapidly decreases with time (Figure 4). For $\epsilon_V^j < 10^{-13} s^{-1}$ and $\eta_\phi = 10^{18} Pa.s$, the reaction rate decreases to zero as a
 405 result of viscoelastic compaction associated with reaction-induced total pressure increase. For $\epsilon_V^j > 10^{-13} s^{-1}$ and $\eta_\phi = 10^{18} Pa.s$, the serpentinisation rate reaches a constant value, indicating, with the formalism adopted in equation 7, that the porosity is constant. The equation for porosity in the system of equations 13 can be solved for a constant dilatational strain rate and a constant
 410 porosity to obtain an equation for the minimum serpentinisation rate:

$$\dot{\xi}_{min} = -\frac{\beta'_s (1 - X_s)}{X_{seq} (1 + \beta_{sr}) (\beta_d (1 - \phi) - \beta'_s)} \frac{\bar{P} - P_w}{(1 - \phi) \eta_\phi} + \frac{\epsilon_V^j (1 - X_s)}{X_{seq} (1 + \beta_{sr})} \quad (14)$$

The analytical solution provided by equation 14 fits well with the constant

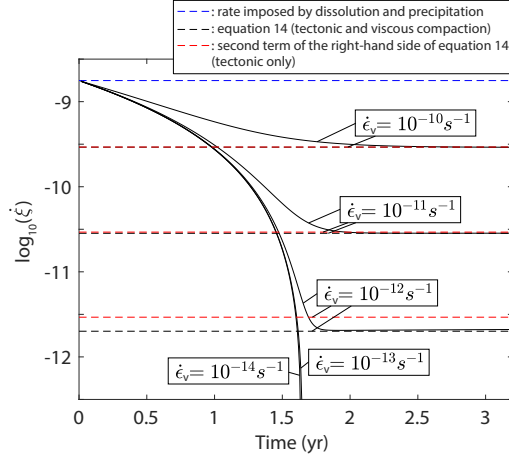


Figure 4: Serpentinisation rate ($\dot{\xi}$) as a function of time for the model considering reaction-induced deformation and an imposed tectonic expansion. The plain black lines corresponds to five simulations performed with $k_{\phi} = 10^{-19} m^2$, $L = 10m$, $\tau = 5 \cdot 10^7 s$, $\eta_{\phi} = 10^{18} Pa.s$, and at the indicated dilatational strain rates ($\epsilon_{\dot{V}}$). The blue dashed line corresponds to the rate imposed by dissolution and precipitation. The black dashed lines corresponds to the rate calculated with equation 14 considering tectonic deformation and viscous compaction. The red dashed lines corresponds to the rate associated with tectonic deformation only and calculated with the second term of right-hand side of equation 14. Note that the serpentinisation rate tends towards the rate imposed by tectonic deformation for $\epsilon_{\dot{V}} > 10^{-13} s^{-1}$.

reaction rate achieved in the numerical simulations (Figure 4), showing that the minimum serpentinisation rate is controlled by a competition between viscous compaction (first term of right-hand side of equation 14) and tectonic expansion (second term of right-hand side of equation 14). Figure 5 provides the time necessary to reach an extent of reaction of 80 % as a function of dilatational strain rate and viscosity (see Supplementary material for details). At low viscosity and low strain rate, reaction does not reach completion as viscous compaction dominates. At moderate to high viscosity and $\epsilon_{\dot{V}} < 3 \cdot 10^{-10} s^{-1}$, the minimum serpentinisation rate is controlled by tectonic deformation. The time to reach 80 % of reaction linearly decreases with strain rate according to the second term of right-hand side of equation 14. It is in the order of millions or thousands of years for $\epsilon_{\dot{V}} = 10^{-13} s^{-1}$ and $\epsilon_{\dot{V}} = 10^{-10} s^{-1}$, respectively. At $\epsilon_{\dot{V}} > 3 \cdot 10^{-10} s^{-1}$, the serpentinisation rate calculated with equation 14 is higher than the rate calculated with equation 7, suggesting that serpentinisation rate is controlled by dissolution and precipitation at the olivine surface.

Estimating if serpentinisation is controlled by reaction-induced deformation or by tectonics is essential to determine if $\dot{\xi}_{max}$ or $\dot{\xi}_{min}$ should be used to model serpentinisation at large scale. Reaction-induced deformation can only occur if the pressure generated during volume expansion is sufficient to induce deformation. The maximum total pressure increase ($\Delta \bar{P}_{max}$) can be derived

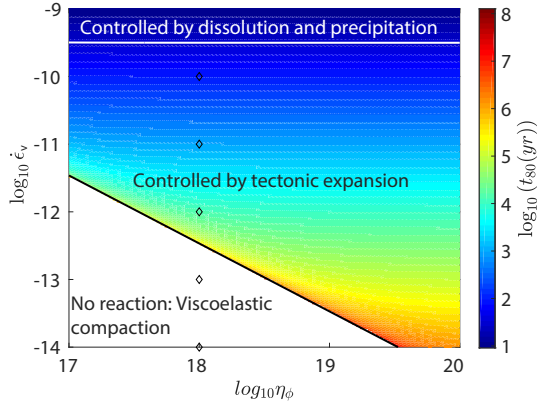


Figure 5: Time necessary to reach 80 % of extent of reaction (t_{80} in years) as a function of viscosity (η_ϕ) and dilatational strain rate (ϵ_V). t_{80} is calculated with equation 14. Three domains can be distinguished: a domain with no reaction due to viscous compaction leading to fluid pathways clogging, tectonic-controlled domain in which the serpentinisation rate can be expressed with the second term of the right-handed side of equation 14, and a dissolution- and precipitation controlled domain in which the rate determined with equation 14 is faster than the one determined with equation 7.

from equation 13 as:

$$\Delta \bar{P}_{max} = -\frac{1 + \beta_{sr}}{\beta_d} \log(1 - \xi X_{seq}) \quad (15)$$

Its values for ξ_{max} and $\xi = 1$ are 14 MPa and ~ 500 MPa, respectively, in good agreement with the maximum value calculated in the volume-controlled simulations (14 MPa at ξ_{max} ; Figure S4). Pressure increase during precipitation (i.e. crystallisation pressure; ΔP_c) has been reported in experiments (Correns, 1949). It is generally calculated in excess of the confining pressure as (Kelemen and Hirth, 2012):

$$\Delta P_c = \frac{RT}{V_m} \log \Omega \quad (16)$$

where Ω is the supersaturation in a thin fluid film where precipitation occurs, R is the gas constant and V_m is the molar volume of the precipitating crystal. ΔP_c values calculated for the serpentinisation reaction can exceed 300 MPa (Kelemen and Hirth, 2012), close to the value of $\Delta \bar{P}_{max}$ at $\xi = 1$. However, equations 15 and 16 are based on different approaches since $\Delta \bar{P}_{max}$ expression considers elastic deformation and depends on the extent of reaction whereas ΔP_c equation is based on thermodynamic disequilibrium between the fluid and the solid and requires the fluid to be significantly supersaturated with respect to the precipitating mineral. Experiments of stress monitoring during hydration show that the reaction-induced pressure increase depends on the extent of reaction, that fluid pathways can shut-down as a result of reaction-induced stress, and that the generated overpressures are generally one order of magnitude smaller

than the one calculated with equation 16 (Wolterbeek et al., 2018; Skarbek et al., 2018). The predictions of our model are in agreement with these results with progressive pressure build-up during reaction, compaction and a relatively small total pressure increase (Figure S4). This suggests that equations 13 are a good
455 alternative to crystallisation pressure calculation based on fluid composition (equation 16), particularly when the supersaturation of the solution is difficult to estimate or when other processes such as mechanical compaction have to be considered. Moreover, it indicates that, for the investigated parameters, the overpressure generated during reaction does not exceed 14 MPa due to viscous
460 compaction (Figure S4). This value is below the yield stress for serpentinised peridotites in compression (Escartín et al., 2001). Our model thus predicts a limited driving force for reaction-induced deformation, which could thus only occur in the first several hundreds of metres below the surface. Figure 5 indicates that serpentinisation may be mainly controlled by tectonic deformation for dilatational strain rates below $3 \cdot 10^{-10} \text{ s}^{-1}$ at mid-ocean ridges. This statement
465 is in agreement with the extensive serpentinisation observed near detachments faults (Rouméjon et al., 2015). Moreover, it validates the approach used in some tectonic models (Bickert et al., 2020) in which serpentinisation rate is related to the strain rate. However, one should keep in mind that shear deformation is
470 not taken into account in Figure 5. We indeed use a constant dilatational strain rate that differs from the shear strain rate computed in previous simulations of mid-ocean ridge processes (Bickert et al., 2020). As a result, we do not capture the potential evolution of strain rate during reaction possibly leading to the switch from one controlling mechanism to another. An accurate modelling
475 of the effect of tectonic deformation on serpentinisation rate would require to determine the extent of strain partitioning during exhumation. This should be achieved in the future by solving for the conservation of total momentum in two or three dimensions and by implementing equation 14 in a compressible code. In addition, the model could be improved by considering aqueous species
480 in the fluid to compute the additional thermodynamic force potentially driving stress build-up (equation 16). Viscous compaction is also modelled here with a formalism derived for macropores (Yarushina and Podladchikov, 2015). However, the nanopores preserved during reaction (Tutolo et al., 2016) may behave differently leading to a different evolution of the porosity through time.

485 The numerical approach proposed here is a critical leap forward in reactive transport modelling since it allows for complete reaction without porosity clogging. Serpentinisation but also other hydration and carbonation reactions inducing a positive change in solid volume can be modelled with the approach proposed here. As a first step, we investigate the volume-controlled and stress-
490 controlled cases but, as shown above, implementing shear stresses will be required in the future to produce quantitative prediction relevant for natural systems. Another improvement of the model concerns the implementation of gas formation (hydrogen and steam). The reaction indeed consumes water, decreasing the fluid pressure to a level sufficient to produce gases at high Da and low
495 De values (Figures S4 B). Vaporisation will in turn significantly modify the fluid density and is thus coupled to fluid pressure evolution. Finally, it would be in-

teresting to distinguish between nano- and macropores in the model. Tutolo et al. (2016) indeed show that nanopores are preserved during serpentinisation whereas macropores can potentially be filled by an assemblage of reaction products and nanopores. This aspect should be considered to accurately model the evolution of the hydraulic properties during reaction and reproduce the evolution of permeability observed in experiments of serpentinisation (Godard et al., 2013; Farough et al., 2015).

Acknowledgements

B.M. acknowledges support from the Swiss National Science Foundation (Grant No. PZ00P2_168083). Y.P. and A.M. were supported by the Russian Ministry of Science and Higher Education (project No. 075-15-2019-1890). We thank Luc Lavier and Lars Rüpke for their thoughtful comments and Jean-Philippe Avouac for editorial handling. B.M. had the idea for the reaction-induced swelling approach aboard Chikyu during the Phase 2 Shipboard Science Party of the Oman Drilling Project. He thanks the members of this Science Party for the stimulating atmosphere aboard.

References

- Balashov, V.N., Yardley, B.W.D., 1998. Modeling metamorphic fluid flow with reaction-compaction-permeability feedbacks. *American Journal of Science* 298, 441–470. URL: <http://www.geology.yale.edu/journals/Ajs.html/http://www.ajsonline.org/cgi/doi/10.2475/ajs.298.6.441>, doi:10.2475/ajs.298.6.441.
- Bayrakci, G., Minshull, T.A., Sawyer, D.S., Reston, T.J., Klaeschen, D., Papenberg, C., Ranero, C., Bull, J.M., Davy, R.G., Shillington, D.J., Perez-Gussinye, M., Morgan, J.K., 2016. Fault-controlled hydration of the upper mantle during continental rifting. *Nature Geoscience* 9, 384–388. URL: www.nature.com/naturegeoscience, doi:10.1038/ngeo2671.
- Beard, J.S., Frost, B.R., Fryer, P., McCaig, A., Searle, R., Ildefonse, B., Zinin, P., Sharma, S.K., 2009. Onset and progression of serpentinization and magnetite formation in Olivine-rich troctolite from IODP hole U1309D. *Journal of Petrology* 50, 387–403. doi:10.1093/petrology/egp004.
- Behn, M.D., Ito, G., 2008. Magmatic and tectonic extension at mid-ocean ridges: 1. Controls on fault characteristics. *Geochemistry, Geophysics, Geosystems* 9, n/a–n/a. URL: <https://agupubs.onlinelibrary.wiley.com/doi/full/10.1029/2008GC001965https://agupubs.onlinelibrary.wiley.com/doi/abs/10.1029/2008GC001965https://agupubs.onlinelibrary.wiley.com/doi/10.1029/2008GC001965http://doi.wiley.com/10.1029/2008GC001965>, doi:10.1029/2008GC001965.

- 535 Bickert, M., Lavier, L., Cannat, M., 2020. How do detachment faults form at
ultraslow mid-ocean ridges in a thick axial lithosphere? *Earth and Planetary
Science Letters* 533, 116048. doi:10.1016/j.epsl.2019.116048.
- Boschi, C., Früh-Green, G.L., Delacour, A., Karson, J.A., Kelley, D.S.,
2006. Mass transfer and fluid flow during detachment faulting and
540 development of an oceanic core complex, Atlantis Massif (MAR
30N). *Geochemistry, Geophysics, Geosystems* 7, n/a–n/a. URL:
[https://agupubs.onlinelibrary.wiley.com/doi/full/10.1029/
2005GC001074](https://agupubs.onlinelibrary.wiley.com/doi/full/10.1029/2005GC001074)[https://agupubs.onlinelibrary.wiley.com/doi/abs/10.
1029/2005GC001074](https://agupubs.onlinelibrary.wiley.com/doi/abs/10.1029/2005GC001074)<https://doi.wiley.com/10.1029/2005GC001074>,
545 doi:10.1029/2005GC001074.
- Boudier, F., Baronnet, A., Mainprice, D., 2010. Serpentine Mineral Re-
placements of Natural Olivine and their Seismic Implications: Oceanic
Lizardite versus Subduction-Related Antigorite. *Journal of Petrology* 51, 495–
512. URL: [https://academic.oup.com/petrology/article-lookup/doi/
10.1093/petrology/egp049](https://academic.oup.com/petrology/article-lookup/doi/10.1093/petrology/egp049), doi:10.1093/petrology/egp049.
- Cannat, M., 1993. Emplacement of mantle rocks in the seafloor at mid-ocean
ridges. *Journal of Geophysical Research* 98, 4163. URL: [http://doi.wiley.
com/10.1029/92JB02221](http://doi.wiley.com/10.1029/92JB02221), doi:10.1029/92JB02221.
- 555 Carmichael, D.M., 1987. Induced Stress and Secondary Mass Transfer:
Thermodynamic Basis for the Tendency toward Constant-Volume Con-
straint in Diffusion Metasomatism, in: *Chemical Transport in Metasomatic
Processes*. Springer Netherlands, Dordrecht, pp. 239–264. URL: [http:
//www.springerlink.com/index/10.1007/978-94-009-4013-0_{_}10](http://www.springerlink.com/index/10.1007/978-94-009-4013-0_{_}10),
560 doi:10.1007/978-94-009-4013-0_10.
- Connolly, J., 2005. Computation of phase equilibria by linear programming: A
tool for geodynamic modeling and its application to subduction zone decar-
bonation. *Earth and Planetary Science Letters* 236, 524–541. URL: [http:
//linkinghub.elsevier.com/retrieve/pii/S0012821X05002839](http://linkinghub.elsevier.com/retrieve/pii/S0012821X05002839)[https:
//linkinghub.elsevier.com/retrieve/pii/S0012821X05002839](https://linkinghub.elsevier.com/retrieve/pii/S0012821X05002839),
565 doi:10.1016/j.epsl.2005.04.033.
- Correns, C.W., 1949. Growth and dissolution of crystals under linear pres-
sure. *Discussions of the Faraday Society* 5, 267. URL: [http://pubs.
rsc.org/en/content/articlehtml/1949/df/df9490500267](http://pubs.rsc.org/en/content/articlehtml/1949/df/df9490500267), doi:10.1039/
570 df9490500267.
- Delescluse, M., Chamot-Rooke, N., 2008. Serpentinization pulse in the actively
deforming Central Indian Basin. *Earth and Planetary Science Letters*
276, 140–151. URL: [http://linkinghub.elsevier.com/retrieve/pii/
S0012821X08005979](http://linkinghub.elsevier.com/retrieve/pii/S0012821X08005979)[https://linkinghub.elsevier.com/retrieve/pii/
S0012821X08005979](https://linkinghub.elsevier.com/retrieve/pii/S0012821X08005979), doi:10.1016/j.epsl.2008.09.017.
575

- Demartin, B., Hirth, G., Evans, B., 2004. Experimental constraints on thermal cracking of peridotite at oceanic spreading centers, in: *Geophysical Monograph Series*. Blackwell Publishing Ltd. volume 148, pp. 167–185. URL: <http://doi.wiley.com/10.1029/148GM07>, doi:10.1029/148GM07.
- 580 Emmanuel, S., Berkowitz, B., 2006. Suppression and stimulation of seafloor hydrothermal convection by exothermic mineral hydration. *Earth and Planetary Science Letters* 243, 657–668. doi:10.1016/j.epsl.2006.01.028.
- Escartín, J., Hirth, G., Evans, B., 1997. Effects of serpentinization on the lithospheric strength and the style of normal faulting at slow-spreading ridges. *Earth and Planetary Science Letters* 151, 181–189. URL: <http://www.sciencedirect.com/science/article/pii/S0012821X9781847X>, doi:10.1016/S0012-821X(97)81847-X.
- 585 Escartín, J., Hirth, G., Evans, B., 2001. Strength of slightly serpentinized peridotites: Implications for the tectonics of oceanic lithosphere. *Geology* 29, 1023–1026. doi:10.1130/0091-7613(2001)029<1023:S0SSPI>2.0.CO.
- 590 Escartín, J., Smith, D.K., Cann, J., Schouten, H., Langmuir, C.H., Escrig, S., 2008. Central role of detachment faults in accretion of slow-spreading oceanic lithosphere. *Nature* 455, 790–794. URL: <https://www.nature.com/articles/nature07333>, doi:10.1038/nature07333.
- 595 Evans, B.W., 1977. Metamorphism of Alpine Peridotite and Serpentinite. *Annual Review of Earth and Planetary Sciences* 5, 397–447. doi:10.1146/annurev.ea.05.050177.002145.
- Evans, O., Spiegelman, M., Kelemen, P.B., 2020. Phase-Field Modeling of Reaction-Driven Cracking: Determining Conditions for Extensive Olivine Serpentinization. *Journal of Geophysical Research: Solid Earth* 125. URL: <https://onlinelibrary.wiley.com/doi/abs/10.1029/2019JB018614>, doi:10.1029/2019JB018614.
- 600 Farough, A., Moore, D.E., Lockner, D.A., Lowell, R.P., 2015. Evolution of fracture permeability of ultramafic rocks undergoing serpentinization at hydrothermal conditions : An experimental study. *Geochemistry, Geophysics, Geosystems* 16, 1–12. doi:10.1002/2015GC005973.Received.
- 605 Fletcher, R.C., Merino, E., 2001. Mineral growth in rocks: Kinetic-rheological models of replacement, vein formation, and syntectonic crystallization. *Geochimica et Cosmochimica Acta* 65, 3733–3748. doi:10.1016/S0016-7037(01)00726-8.
- 610 Germanovich, L.N., Genc, G., Lowell, R.P., Rona, P.a., 2012. Deformation and surface uplift associated with serpentinization at mid-ocean ridges and subduction zones. *Journal of Geophysical Research* 117, B07103. URL: <http://doi.wiley.com/10.1029/2012JB009372>, doi:10.1029/2012JB009372.

- 615 Godard, M., Luquot, L., Andreani, M., Gouze, P., 2013. Incipient hydration of mantle lithosphere at ridges: A reactive-percolation experiment. *Earth and Planetary Science Letters* 371-372, 92–102. URL: <http://linkinghub.elsevier.com/retrieve/pii/S0012821X13001799>, doi:10.1016/j.epsl.2013.03.052.
- 620 Hilairt, N., Reynard, B., Wang, Y., Daniel, I., Merkel, S., Nishiyama, N., Petitgirard, S., 2007. High-Pressure Creep of Serpentine, Interseismic Deformation, and Initiation of Subduction. *Science* 318, 1910–1913. URL: <http://www.sciencemag.org/cgi/doi/10.1126/science.1148494>, doi:10.1126/science.1148494.
- 625 Iyer, K., Rüpke, L.H., Morgan, J.P., 2010. Feedbacks between mantle hydration and hydrothermal convection at ocean spreading centers. *Earth and Planetary Science Letters* 296, 34–44. doi:10.1016/j.epsl.2010.04.037.
- Jamtveit, B., Putnis, C.V., Malthe-Sørenssen, A., 2009. Reaction induced fracturing during replacement processes. *Contributions to Mineralogy and Petrology* 157, 127–133. URL: <http://link.springer.com/article/10.1007/s00410-008-0324-y>, doi:10.1007/s00410-008-0324-y.
- 630 Kelemen, P.B., Hirth, G., 2012. Reaction-driven cracking during retrograde metamorphism: Olivine hydration and carbonation. *Earth and Planetary Science Letters* 345-348, 81–89. URL: <http://www.sciencedirect.com/science/article/pii/S0012821X12003020><http://dx.doi.org/10.1016/j.epsl.2012.06.018>, doi:10.1016/j.epsl.2012.06.018.
- 635 Kelley, C.T., Keyes, D.E., 1998. Convergence Analysis of Pseudo-Transient Continuation. *SIAM Journal on Numerical Analysis* 35, 508–523. URL: <http://epubs.siam.org/doi/10.1137/S0036142996304796>, doi:10.1137/S0036142996304796.
- 640 Kieffer, B., Jové, C.F., Oelkers, E.H., Schott, J., 1999. An experimental study of the reactive surface area of the Fontainebleau sandstone as a function of porosity, permeability, and fluid flow rate. *Geochimica et Cosmochimica Acta* 63, 3525–3534. doi:10.1016/S0016-7037(99)00191-X.
- 645 Klein, F., Le Roux, V., 2020. Quantifying the volume increase and chemical exchange during serpentization. *Geology* URL: <https://pubs.geoscienceworld.org/gsa/geology/article/583188/Quantifying-the-volume-increase-and-chemical>, doi:10.1130/G47289.1.
- 650 Lafay, R., Montes-Hernandez, G., Janots, E., Chiriac, R., Findling, N., Toche, F., 2012. Mineral replacement rate of olivine by chrysotile and brucite under high alkaline conditions. *Journal of Crystal Growth* 347, 62–72. URL: <http://dx.doi.org/10.1016/j.jcrysgro.2012.02.040>, doi:10.1016/j.jcrysgro.2012.02.040.

- 655 Lichtner, P.C., 1988. The quasi-stationary state approximation to coupled mass transport and fluid-rock interaction in a porous medium. *Geochimica et Cosmochimica Acta* 52, 143–165. URL: <http://linkinghub.elsevier.com/retrieve/pii/0016703788900634>, doi:10.1016/0016-7037(88)90063-4.
- 660 Liu, D., Agarwal, R., Li, Y., Yang, S., 2019. Reactive transport modeling of mineral carbonation in unaltered and altered basalts during CO₂ sequestration. *International Journal of Greenhouse Gas Control* 85, 109–120. URL: <https://linkinghub.elsevier.com/retrieve/pii/S1750583618309009>, doi:10.1016/j.ijggc.2019.04.006.
- 665 Llana-Fúnez, S., Brodie, K.H., Rutter, E.H., Arkwright, J.C., 2007. Experimental dehydration kinetics of serpentinite using pore volumetry. *Journal of Metamorphic Geology* 25, 423–438. URL: <http://doi.wiley.com/10.1111/j.1525-1314.2007.00703.x>, doi:10.1111/j.1525-1314.2007.00703.x.
- 670 Macdonald, A., Fyfe, W., 1985. Rate of serpentinization in seafloor environments. *Tectonophysics* 116, 123–135. URL: <https://linkinghub.elsevier.com/retrieve/pii/0040195185902252>, doi:10.1016/0040-1951(85)90225-2.
- Malvoisin, B., Austrheim, H., Hetényi, G., Reynes, J., Hermann, J., Baumgartner, L.P., Podladchikov, Y.Y., 2020a. Sustainable densification of the deep crust. *Geology* 48, 673–677. doi:10.1130/G47201.1.
- 675 Malvoisin, B., Brantut, N., Kaczmarek, M.A., 2017. Control of serpentinisation rate by reaction-induced cracking. *Earth and Planetary Science Letters* 476, 143–152. URL: <https://linkinghub.elsevier.com/retrieve/pii/S0012821X17304260>, doi:10.1016/j.epsl.2017.07.042.
- 680 Malvoisin, B., Brunet, F., Carlut, J., Rouméjon, S., Cannat, M., 2012a. Serpentinization of oceanic peridotites: 2. Kinetics and processes of San Carlos olivine hydrothermal alteration. *Journal of Geophysical Research: Solid Earth* 117, n/a–n/a. URL: <http://doi.wiley.com/10.1029/2011JB008842>, doi:10.1029/2011JB008842.
- 685 Malvoisin, B., Carlut, J., Brunet, F., 2012b. Serpentinization of oceanic peridotites: 1. A high-sensitivity method to monitor magnetite production in hydrothermal experiments. *Journal of Geophysical Research: Solid Earth* 117. doi:10.1029/2011JB008612.
- 690 Malvoisin, B., Podladchikov, Y.Y., Vrijmoed, J.C.J., 2015. Coupling changes in densities and porosity to fluid pressure variations in reactive porous fluid flow: Local thermodynamic equilibrium. *Geochemistry Geophysics Geosystems* 16, 1–57. URL: <http://doi.wiley.com/10.1002/2015GC006019><http://onlinelibrary.wiley.com/doi/10.1002/2015GC006019/full>, doi:10.1002/2015GC006019.

- 695 Malvoisin, B., Zhang, C., Müntener, O., Baumgartner, Lukas, P., Kelemen,
P.B., Oman Drilling Project Science Party, 2020b. Measurement of volume
change and mass transfer during serpentinisation: insights from the Oman
Drilling Project. *Journal of Geophysical Research: Solid Earth* .
- 700 Marini, L., 2007. Geological Sequestration of Carbon Dioxide: Thermody-
namics, Kinetics, and Reaction Path Modeling, in: *Geological Sequestration
of Carbon Dioxide: Thermodynamics, Kinetics, and Reaction Path
Modeling*. Elsevier. volume 11, pp. 319–409. URL: [https://books.
google.ch/books?hl=fr&lr=&id=7GpCbfi7oUQC&oi=fnd&pg=
PP1&dq=marini+2007+CO2+sequestration&ots=DNDqYwZfCL&sig=
DHPz3m3MXXrVmSeANLRgiU6Lpj0http://www.sciencedirect.com/
705 science/article/pii/S0921319806800268%5Cnhttp://books.google.
com/books?hl=en,doi:10.1016/S0921-3198\(06\)80023-2](https://books.google.ch/books?hl=fr&lr=&id=7GpCbfi7oUQC&oi=fnd&pg=PP1&dq=marini+2007+CO2+sequestration&ots=DNDqYwZfCL&sig=DHPz3m3MXXrVmSeANLRgiU6Lpj0http://www.sciencedirect.com/science/article/pii/S0921319806800268%5Cnhttp://books.google.com/books?hl=en,doi:10.1016/S0921-3198(06)80023-2).
- Martin, B., Fyfe, W., 1970. Some experimental and theoret-
ical observations on the kinetics of hydration reactions with par-
ticular reference to serpentinization. *Chemical Geology* 6, 185–
710 202. URL: [http://www.sciencedirect.com/science/article/pii/
0009254170900185](http://www.sciencedirect.com/science/article/pii/0009254170900185), doi:10.1016/0009-2541(70)90018-5.
- McCollom, T.M., Seewald, J.S., 2013. Serpentinites, Hydrogen, and Life. *El-
ements* 9. URL: [http://elements.geoscienceworld.org/content/9/2/
129](http://elements.geoscienceworld.org/content/9/2/129).
- 715 O’Hanley, D.S., 1992. Solution to the volume problem in serpentinization. *Geol-
ogy* 20, 705–708. doi:10.1130/0091-7613(1992)020<0705:STTVPI>2.3.CO.
- Omlin, S., Malvoisin, B., Podladchikov, Y.Y., 2017. Pore Fluid Extraction
by Reactive Solitary Waves in 3-D. *Geophysical Research Letters* 44, 9267–
9275. URL: <http://doi.wiley.com/10.1002/2017GL074293>, doi:10.1002/
720 2017GL074293.
- Oufi, O., 2002. Magnetic properties of variably serpentinized abyssal peri-
dotites. *Journal of Geophysical Research* 107. URL: [http://www.agu.org/
pubs/crossref/2002/2001JB000549.shtml](http://www.agu.org/pubs/crossref/2002/2001JB000549.shtml), doi:10.1029/2001JB000549.
- Paukert, A., 2014. Mineral Carbonation in Mantle Peridotite of the Samail
725 Ophiolite , Oman : Implications for permanent geological carbon dioxide
capture and storage , 166doi:10.7916/D85M63WZ.
- Plümper, O., Røyne, A., Magrasó, A., Jamtveit, B., 2012. The interface-scale
mechanism of reaction-induced fracturing during serpentinization. *Geology*
40, 1103–1106. doi:10.1130/G33390.1.
- 730 Ranero, C.R., Phipps Morgan, J., McIntosh, K., Relchert, C., 2003.
Bending-related faulting and mantle serpentinization at the Middle Amer-
ica trench. *Nature* 425, 367–373. URL: [https://pubmed.ncbi.nlm.nih.
gov/14508480/](https://pubmed.ncbi.nlm.nih.gov/14508480/), doi:10.1038/nature01961.

- 735 Rouméjon, S., Cannat, M., Agrinier, P., Godard, M., Andreani, M., 2015. Serpentinization and Fluid Pathways in Tectonically Exhumed Peridotites from the Southwest Indian Ridge (62-65 E). *Journal of Petrology* 56, 703–734. URL: <https://academic.oup.com/petrology/article-lookup/doi/10.1093/petrology/egv014>, doi:10.1093/petrology/egv014.
- 740 Rudge, J.F., Kelemen, P.B., Spiegelman, M., 2010. A simple model of reaction-induced cracking applied to serpentinization and carbonation of peridotite. *Earth and Planetary Science Letters* 291, 215–227. URL: <http://linkinghub.elsevier.com/retrieve/pii/S0012821X10000452>, doi:10.1016/j.epsl.2010.01.016.
- 745 Rüpke, L.H., Hasenclever, J., 2017. Global rates of mantle serpentinization and H₂ production at oceanic transform faults in 3-D geodynamic models. *Geophysical Research Letters* 44, 6726–6734. URL: <http://doi.wiley.com/10.1002/2017GL072893>, doi:10.1002/2017GL072893.
- 750 Russell, M.J., Hall, A.J., Martin, W., 2010. Serpentinization as a source of energy at the origin of life. *Geobiology* 8, 355–371. URL: <http://doi.wiley.com/10.1111/j.1472-4669.2010.00249.x>, doi:10.1111/j.1472-4669.2010.00249.x.
- 755 Schmalholz, S.M., Moulas, E., Plümper, O., Myasnikov, A.V., Podladchikov, Y.Y., 2020. 2D HydroMechanicalChemical modelling of (de)hydration reactions in deforming heterogeneous rock: The periclasebrucite model reaction. *Geochemistry, Geophysics, Geosystems* URL: <https://onlinelibrary.wiley.com/doi/10.1029/2020GC009351>, doi:10.1029/2020GC009351.
- 760 Schroeder, T., John, B.E., 2004. Strain localization on an oceanic detachment fault system, Atlantis Massif, 30N, Mid-Atlantic Ridge. *Geochemistry, Geophysics, Geosystems* 5, n/a–n/a. URL: <https://agupubs.onlinelibrary.wiley.com/doi/full/10.1029/2004GC000728><https://agupubs.onlinelibrary.wiley.com/doi/abs/10.1029/2004GC000728><https://agupubs.onlinelibrary.wiley.com/doi/10.1029/2004GC000728><http://doi.wiley.com/10.1029/2004GC000728>, doi:10.1029/2004GC000728.
- 765 Shimizu, H., Okamoto, A., 2016. The roles of fluid transport and surface reaction in reaction-induced fracturing, with implications for the development of mesh textures in serpentinites. *Contributions to Mineralogy and Petrology* 171, 73. URL: <http://link.springer.com/10.1007/s00410-016-1288-y>, doi:10.1007/s00410-016-1288-y.
- 770 Skarbek, R.M., Savage, H.M., Kelemen, P.B., Yancopoulos, D., 2018. Competition Between Crystallization-Induced Expansion and Creep Compaction During Gypsum Formation, and Implications for Serpentinization. *Journal of Geophysical Research: Solid Earth* 123, 5372–5393. URL: <http://doi.wiley.com/10.1029/2017JB015369>, doi:10.1029/2017JB015369.

- 775 Szitkar, F., Dymant, J., Fouquet, Y., Honsho, C., Horen, H., 2014. The mag-
netic signature of ultramafic-hosted hydrothermal sites. *Geology* 42, 715–718.
doi:10.1130/G35729.1.
- Thayer, T.P., 1966. Serpentinization considered as a constant-volume
metasomatic process. *The American mineralogist* 51, 685–710. URL:
780 [https://pubs.geoscienceworld.org/msa/ammin/article-abstract/51/
5-6/685/540300](https://pubs.geoscienceworld.org/msa/ammin/article-abstract/51/5-6/685/540300).
- Tian, M., Ague, J.J., 2014. The impact of porosity waves on crustal reac-
tion progress and CO₂ mass transfer. *Earth and Planetary Science Letters*
390, 80–92. URL: <http://dx.doi.org/10.1016/j.epsl.2013.12.044>
785 <http://linkinghub.elsevier.com/retrieve/pii/S0012821X13007590>, doi:10.
1016/j.epsl.2013.12.044.
- Tian, M., Ague, J.J., Chu, X., Baxter, E.F., Dragovic, N., Chamberlain, C.P.,
Rumble, D., 2018. The Potential for Metamorphic Thermal Pulses to Develop
During Compaction-Driven Fluid Flow. *Geochemistry, Geophysics, Geosys-*
790 *tems* 19, 232–256. URL: <http://doi.wiley.com/10.1002/2017GC007269>,
doi:10.1002/2017GC007269.
- Tutolo, B.M., Mildner, D.F., Gagnon, C.V., Saar, M.O., Seyfried,
W.E., 2016. Nanoscale constraints on porosity generation and
fluid flow during serpentinization. *Geology* 44, 103–106. URL:
795 <http://geology.gsapubs.org/content/44/2/103.shorthttps://pubs.geoscienceworld.org/geology/article/44/2/103-106/132000>,
doi:10.1130/G37349.1.
- Ulven, O., Jamtveit, B., Malthe-Sørensen, A., 2014. Reaction-driven fracturing
of porous rock. *Journal of Geophysical Research: Solid Earth* 119, 7473–
800 7486. URL: <http://doi.wiley.com/10.1002/2014JB011102>, doi:10.1002/
2014JB011102.
- Van Avendonk, H.J., Holbrook, W.S., Lizarralde, D., Denyer, P., 2011.
Structure and serpentinization of the subducting Cocos plate offshore
Nicaragua and Costa Rica. *Geochemistry, Geophysics, Geosystems* 12.
805 URL: [https://agupubs.onlinelibrary.wiley.com/doi/full/10.1029/
2011GC003592https://agupubs.onlinelibrary.wiley.com/doi/abs/10.
1029/2011GC003592https://agupubs.onlinelibrary.wiley.com/doi/
10.1029/2011GC003592](https://agupubs.onlinelibrary.wiley.com/doi/full/10.1029/2011GC003592https://agupubs.onlinelibrary.wiley.com/doi/abs/10.1029/2011GC003592https://agupubs.onlinelibrary.wiley.com/doi/10.1029/2011GC003592), doi:10.1029/2011GC003592.
- Wolterbeek, T.K., van Noort, R., Spiers, C.J., 2018. Reaction-driven casing
expansion: potential for wellbore leakage mitigation. *Acta Geotechnica* 13,
810 341–366. doi:10.1007/s11440-017-0533-5.
- Xu, T., Spycher, N., Sonnenthal, E., Zhang, G., Zheng, L., Pruess, K., 2011.
Toughreact version 2.0: A simulator for subsurface reactive transport under
non-isothermal multiphase flow conditions. *Computers and Geosciences* 37,
763–774. doi:10.1016/j.cageo.2010.10.007.

- 815 Yarushina, V.M., Podladchikov, Y.Y., 2015. (De)compaction of porous viscoelastoplastic media: Model formulation. *Journal of Geophysical Research: Solid Earth* 120, 4146–4170. URL: <http://doi.wiley.com/10.1002/2014JB011258>, doi:10.1002/2014JB011258.
- 820 Zhang, L., Nasika, C., Donzé, F., Zheng, X., Renard, F., Scholtès, L., 2019. Modeling Porosity Evolution Throughout ReactionInduced Fracturing in Rocks With Implications for Serpentinization. *Journal of Geophysical Research: Solid Earth* 124, 5708–5733. URL: <https://onlinelibrary.wiley.com/doi/abs/10.1029/2018JB016872>, doi:10.1029/2018JB016872.